Two-way coupling in shear layers with dilute bubble concentrations

G. R. Ruetsch[a] and E. Meiburg
Department of Aerospace Engineering, University of Southern California, Los Angeles, California 90089-1191

(Received 21 September 1993; accepted 27 April 1994)

Direct numerical simulations are used to analyze the evolution of a temporally growing two-dimensional shear layer seeded with dilute concentrations of bubbles under gravity. The bubble concentrations are dilute enough so that bubble–bubble interactions can be neglected, but are large enough for cumulative effects of bubbles to influence the flow. The evolution of the bubble field is determined by tracking many individual bubbles, and the flow field is advanced by using the Navier–Stokes equations with a coupling term representing the effect of the bubbles on the flow. The results are interpreted in terms of the vorticity, density, and pressure fields relative to the one-way coupled or passive case. For the coupled case, a reduction in the magnitude of the vorticity and pressure gradients near the vortex center is observed. In addition to modification of the flow, it is observed that the accumulation of bubbles is smaller and the location of the equilibrium points are shifted farther from the vortex center as a result of the coupling. It is explored how these changes are modified by different Froude numbers and bubble sizes. The differences between passive and coupled cases usually increase due to larger accumulations as larger bubbles are considered. However, for certain Froude numbers an optimum coupling is observed at intermediate bubble sizes due to the absence of equilibrium points for large bubbles.

I. INTRODUCTION

One important and common feature that occurs in a variety of fluid systems is the presence of shear layers. The evolution of shear layers has received much attention by researchers, due to the critical role it plays in mixing, momentum transport, and transition to turbulence. As a result, there have been many advances in understanding the nature of single phase shear layers, such as the observation of coherent spanwise structures that arise from Kelvin–Helmholtz instabilities,[1,2] and the three-dimensional structures that arise when these spanwise structures become unstable.[3,4]

Recently, the behavior of small particles in shear layers has been investigated. The applications of such studies are far reaching, ranging from the mixing of fuel in engines to the dispersion of pollutants in the environment. The nature of this advection depends on the density of the particles relative to the fluid of the shear layer. On one hand, dispersion of heavy or aerosol particles occurs when these particles are introduced into shear layers, which is observed both in experiments[5,6] and simulations.[7,8] On the other hand, particles that are lighter than the carrier fluid, such as air bubbles in water, accumulate near the center of vortices in cellular flows[9] and in temporally evolving shear layers.[10] One common assumption made in all the previously mentioned numerical studies is to only consider dilute suspensions of particles. This assumption allows one to neglect the interactions between particles and the fluid and among particles themselves.

There have been several approaches to studying nondilute particle-laden flows. For example, Biesheuvel and Gorrisen[11] use a kinetic theory approach to derive one-dimensional conservation equations in their investigation of void fraction disturbances for the case of large bubbles at large void fractions. Cook and Harlow[12] employed ensemble-averaged two-field equations with various closure models to investigate a bubble-laden von Kármán vortex street.

In this study, we wish to consider "weakly dilute" suspensions of bubbles, namely flows with bubbles that are dilute enough so that bubble–bubble interactions can be neglected, but not dilute enough to ignore cumulative effects of bubbles on the flow. We also wish to do this in a direct fashion, to avoid making assumptions about closure models. A similar approach has been used for heavy particles in the simulations of Squires and Eaton,[13] and most recently Elghobashi and Truesdell,[14] who investigated turbulence modification by particles by including a source of momentum in the Navier–Stokes equations which accounts for the net force on the particles back on the fluid. We use this approach for the case of bubbles, which, due to their massless nature, yield a different contribution to the momentum equations of the flow.

In the next section, we discuss the governing equations for the bubble motion and then derive the momentum equations for the flow, making use of the weakly dilute assumption in a general context. We then discuss the particular flow configuration we pursue in this study. A brief discussion of the numerical methods and methods for analysis of the data are presented, followed by the results of the simulations.

II. GOVERNING EQUATIONS

The flow we are considering concerns the motion of a dilute concentration of gas bubbles in a liquid, such as water. Our approach to this problem is to solve equations governing each phase which incorporate the effects from the other phase, resulting in a two-way coupling. Throughout this sec-

[a]Present address: Center for Turbulence Research, Stanford University, Stanford, California 94305.

 1070-6631/94/6(8)/2656/15/$6.00 © 1994 American Institute of Physics

Downloaded 22 May 2004 to 128.111.70.70. Redistribution subject to AIP license or copyright, see http://pof.aip.org/pof/copyright.jsp

tion we refer to the gas bubbles as either the bubble or particle phase and the water or liquid as the fluid phase.

Unlike other studies, our goal is not to derive field equations for both phases. We derive field equations only for the fluid phase, and calculate the bubble phase by following discrete bubbles. The equations discussed in this section apply to any weakly dilute bubbly flow. We specify these equations to our particular flow field and provide initial conditions in a later section.

A. Bubble equation

We begin by discussing the equations used to calculate the bubble trajectories in the fluid. Depending on the flow conditions around the bubble, there are several different equations one can use here. In this study we consider bubbles small enough such that they are dominated by viscous forces, and consider surface tension large enough to assume a spherical shape with constant volume. Due to the presence of surface impurities common in many flows of interest, we can further assume that the bubbles behave as solid rigid spheres.[15,9,16] This last assumption is important in determining the expression for the drag force. For a rigid sphere, the drag is given by the Stokes drag law, $6\pi a\mu(u_i-V_i)$, and the drag force on a bubble using stress-free boundary conditions is given by $4\pi a\mu(u_i-V_i)$. (In these expressions a is the bubble radius, u_i is the undisturbed fluid velocity, V_i is the bubble velocity, and μ is the fluid viscosity.) For bubbles that satisfy these assumptions listed above, we can use the equation of motion derived by Maxey and Riley[17] for particles in general, which neglecting the Faxen corrections for a nonuniform flow is given by

$$m_p\frac{dV_i}{dt}=(m_f-m_p)g\delta_{3i}+m_f\frac{Du_i}{Dt}+\frac{1}{2}m_f\left(\frac{Du_i}{Dt}-\frac{dV_i}{dt}\right)+6\pi a\mu(u_i-V_i)+6\pi a^2\mu\int_0^t\frac{d(u_i-V_i)/d\tau}{\sqrt{\pi\nu(t-\tau)}}d\tau, \tag{1}$$

where m_f and m_p are the mass of the fluid displaced by the particle and the mass of the particle. Here we have assumed that the acceleration of gravity g points in the negative x_3 direction. The terms on the right-hand side of Eq. (1) represent the gravitational force, pressure force in absence of the particle, the added mass effects of the form given by Auton *et al.*,[18] Stokes drag, and the Basset history term. In addition to neglecting the Faxen corrections, we also choose to neglect the Basset history term. The basis for doing so lies in the assumptions used to derive Eq. (1), where the Reynolds number based on the particle radius and slip velocity, u_i-V_i, is zero. Departures from this condition have been determined to result in a more quickly decaying kernel of the Basset history term.[19]

We nondimensionalize Eq. (1) with U and δ (not to be confused with the Kronecker delta, δ_{ij}, used above in the gravitational term) as the velocity and length scales, and using the notation of Maxey[9] we obtain the following equation for the acceleration of the particle:

$$\frac{dV_i}{dt}=\mathscr{A}(u_i+\mathscr{W}\delta_{3i}-V_i)+\frac{3}{2}\mathscr{R}\frac{Du_i}{Dt}. \tag{2}$$

We have introduced three nondimensional parameters in Eq. (2), $\mathscr{A}$, $\mathscr{R}$, and $\mathscr{W}$. The settling velocity parameter, $\mathscr{W}$, is defined as

$$\mathscr{W}=\frac{(m_f-m_p)g}{6\pi a\mu U},$$

and represents the ratio of gravitational to viscous effects, where $\mathscr{W}U$ gives the terminal rise/settling velocity of a particle in a still fluid. The mass ratio parameter, $\mathscr{R}$, is defined as

$$\mathscr{R}=\frac{\rho_f}{\rho_p+\frac{1}{2}\rho_f},$$

and reflects the difference between the fluid and particle densities. The material derivative in Eq. (2) represents the effect of the pressure gradients on the particle motion, and therefore $\mathscr{R}$ plays a crucial role in determining how particle and fluid element trajectories differ. The mass ratio parameter can cover the range of $0\leqslant\mathscr{R}\leqslant 2$. For $\mathscr{R}=\frac{2}{3}$, the pressure has the same effect on the particle as on a fluid element, and corresponds to the case of neutrally buoyant particles. For $\mathscr{R}=0$, corresponding to heavy particles, the pressure forces have no effect on the particle motion. For bubbles with $\mathscr{R}=2$, the pressure forces are three times as important to the bubble motion relative to a fluid element. It is for this reason that heavy particles are dispersed by vortices while bubbles are entrapped by vortices. In this study, we consider only bubbles with $\mathscr{R}=2$.

The inertia parameter, $\mathscr{A}$, is defined as

$$\mathscr{A}=\frac{6\pi a\mu\delta}{(m_p+\frac{1}{2}m_f)U},$$

and is the inverse of the Stokes number. The inertia parameter reflects the relative importance of viscous to inertial effects, and in this study is large, reflecting the dominance of the viscous forces.

At this point we should comment on the credibility of using the Stokes drag law in Eqs. (1) and (2). One requisite for using this expression is that the Reynolds number based on the slip velocity and particle diameter be small:

$$\mathrm{Re}_p=\frac{|\mathbf{u}-\mathbf{V}|2a}{\nu}\ll 1.$$

In the absence of gravitational effects this restriction is met for the values of $\mathscr{A}$ we consider here, but since we are interested in cases where $\mathscr{W}\neq 0$ this condition can be violated. We can correct this using an empirical coefficient based on Re_p from Clift *et al.*:[15]

$$f=1.0+0.15\ \mathrm{Re}_p^{2/3},$$

which results in the following equation:

$$\frac{dV_i}{dt}=f\mathscr{A}(u_i-V_i)+\mathscr{A}\mathscr{W}\delta_{3i}+\frac{3}{2}\mathscr{R}\frac{Du_i}{Dt}. \tag{3}$$

Downloaded 22 May 2004 to 128.111.70.70. Redistribution subject to AIP license or copyright, see http://pof.aip.org/pof/copyright.jsp

In addition to altering the drag term, the nonzero rise velocity further justifies the elimination of the Basset-history term from this equation due to the finite Reynolds number effects.

In developing Eq. (3), we have assumed that only a single bubble is present. But since we are dealing with a weakly dilute suspension of bubbles, the bubble–bubble interactions are neglected, and we can calculate each bubble trajectory using Eq. (3) independently.

B. Fluid equations

In this section we derive the governing equations that describe the evolution of the fluid phase. Since we are concerned with the motion of air bubbles in an incompressible liquid, we begin the analysis of the governing equations for the fluid phase with the incompressible Navier–Stokes equations:

$$\frac{\partial u_i}{\partial x_i}=0, \tag{4}$$

$$\rho_f \frac{Du_i}{Dt}=-\frac{\partial P}{\partial x_i}-\rho_f g\,\delta_{3i}+\mu\frac{\partial^2 u_i}{\partial x_j^2}+b_i, \tag{5}$$

where P is the pressure and b_i is the force of the bubbles on the fluid. We can determine b_i from the equation of motion for a single bubble, Eq. (1), which can be restated as

$$m_p\frac{dV_i}{dt}=\mathcal{F}_i+\mathcal{S}_i=0,$$

where the last equality results from substituting $m_p=0$ in the first term. Here $\mathcal{F}_i$ and $\mathcal{S}_i$ represent the net body and surface forces on the bubble. From Eq. (1), we obtain $\mathcal{F}_i=m_f g\,\delta_{3i}$, and $\mathcal{S}_i$ consists of all the other terms on the right-hand side of the equation. It is important to differentiate between these body and surface forces, since Newton's third law of action–reaction implies that the force exerted by a single bubble on the fluid is simply

$$B_i=-\mathcal{S}_i=\mathcal{F}_i=\rho_f C g\,\delta_{3i},$$

where $C=\frac{4}{3}\pi a^3$ is the volume of the bubble. The coupling term b_i in the momentum equation exists at the bubble interface, but rather than calculate the interaction between phases in such a fashion we choose a more macroscopic approach. For N bubbles under the weakly dilute assumption, we obtain the overall force as

$$\sum_N B_i=N\rho_f\bar{C}g\,\delta_{3i},$$

where $\bar{C}$ is the average volume of the bubbles. This extensive quantity can then be converted to the average intensive force $\bar{b}_i$ by dividing by the total volume:

$$\bar{b}_i=\bar{\eta}\bar{C}\rho_f g\,\delta_{3i},$$

where $\bar{\eta}$ is the global or average number density, defined as the number of bubbles per volume. We can also use the average void fraction,

$$\bar{\epsilon}=\bar{\eta}\bar{C},$$

in this expression:

$$\bar{b}_i=\bar{\epsilon}\rho_f g\,\delta_{3i}.$$

Although this force applies only at the fluid–bubble interface, for our macroscopic approach we can define the local force of the bubbles on the fluid as

$$b_i=\epsilon\rho_f g\,\delta_{3i},$$

where ϵ is the local void fraction. Using this expression for the force per unit volume of the bubbles on the fluid, we can write Eq. (5) as

$$\rho_f\frac{Du_i}{Dt}=-\frac{\partial P}{\partial x_i}+\mu\frac{\partial^2 u_i}{\partial x_j^2}-(1-\epsilon)\rho_f g\,\delta_{3i}. \tag{6}$$

We can interpret the last term of Eq. (6) in terms of the density of the fluid–bubble mixture, which is given by

$$\rho=\rho_f(1-\epsilon). \tag{7}$$

From Eqs. (6) and (7), we see that the net effect of the weakly dilute suspension of bubbles is to introduce a buoyancy term, which is a function of the local void fraction.

The next step is to determine the reference state of the fluid obtained by setting $u_i=0$ and $\epsilon=\bar{\epsilon}$ in Eq. (6):

$$0=-\frac{\partial P_0}{\partial x_i}-\rho_0 g\,\delta_{3i}.$$

For cases with $\bar{\epsilon}=0$ and thus $\bar{b}_i=0$, we obtain the familiar hydrostatic equation, where $\rho_0=\rho_f$. However, in our case this procedure yields a reference density, given by

$$\rho_0=\rho_f(1-\bar{\epsilon}),$$

or simply the average density of the fluid–bubble mixture. Using this relation with Eq. (7), we can define the perturbation density of the mixture as

$$\rho'=\rho-\rho_0=\rho_f(\bar{\epsilon}-\epsilon). \tag{8}$$

If we now make the substitution $P=P_0+P'$, subtract the reference state from Eq. (6), divide by ρ_f, and nondimensionalize Eqs. (4), (6), and (8) according to the following variables:

$$u^+=\frac{u}{U},\quad x^+=\frac{x}{\delta},\quad t^+=\frac{tU}{\delta};$$

$$\rho^+=\frac{\rho}{\rho_f},\quad \epsilon^+=\frac{\epsilon}{\bar{\epsilon}},\quad P^+=\frac{P}{(\rho_f U^2)};$$

we obtain the following set of equations, with the +'s omitted:

$$\frac{\partial u_i}{\partial x_i}=0, \tag{9}$$

$$\frac{Du_i}{Dt}=-\frac{\partial P'}{\partial x_i}+\frac{1}{\mathrm{Re}}\frac{\partial^2 u_i}{\partial x_j^2}-\frac{1}{\mathcal{F}^2}\rho'\,\delta_{3i}, \tag{10}$$

$$\rho'=\bar{\epsilon}(1-\epsilon). \tag{11}$$

In addition to including $\bar{\epsilon}$ in this set of equations, we have also introduced two additional parameters, the Reynolds and Froude numbers, given by

$$\mathrm{Re}=U\delta/\nu;\quad \mathcal{F}=U/(g\delta)^{1/2}.$$

Downloaded 22 May 2004 to 128.111.70.70. Redistribution subject to AIP license or copyright, see http://pof.aip.org/pof/copyright.jsp

We should point out several features concerning Eqs. (9)–(11). The most obvious is that Eq. (10) is the same equation that one obtains in a fluid of variable density under the Boussinesq approximation. The Boussinesq approximation assumes that density variations are small enough so that the density appears as a constant in all terms except the buoyancy term. These are the same assumptions we made when specifying our fundamental equations, so the fact that we obtain the Boussinesq equations is no surprise. The difference between a Boussinesq fluid and our two-phase flow is that in the case of the former the density or temperature field is determined by a convection–diffusion equation, whereas for the two-phase flow the density field is a function of the void fraction, Eq. (11), which is in turn dependent on the equation of motion for the bubbles, Eq. (3). We should also point out some features that are not present in Eqs. (9)–(11). There are corrections due to the Reynolds stresses and effective viscosity that also play a role in the evolution of the flow. These effects are present for even small void fractions, but are not included in the present study. The reason for their omission is that we wish to study fundamental mechanisms that occur in a two-way coupled flow. The effective viscosity and Reynolds stresses would make a quantitative difference in the mechanisms, but the overall qualitative features would remain unchanged.

III. FLOW CONFIGURATION

In the previous section we discussed the set of equations needed to solve for each component of a two-phase flow. In developing these equations we left the flow length and velocity scales, δ and U, undetermined, since we wished to emphasize the fact that these equations are valid for any weakly dilute bubbly flow. Having done this, we now turn our attention to the specific flow we consider.

The flow configuration we study is a two-dimensional shear layer initially with a parallel flow in the x_1 direction and gravity acting in the negative x_3 direction. This base flow has a tanh velocity profile, and is perturbed using eigenfunctions corresponding to the most unstable mode of inviscid theory.[20] The velocity scale U is the velocity difference across the shear layer, and the length scale δ is taken to be the vorticity thickness, defined as

$$\delta=\frac{U}{(\partial u/\partial x_3)_{\max}}.$$

For these scales, the nondimensional initial profile is given by

$$u(x_3)=\tfrac{1}{2}\tanh(2x_3),$$

and the initial perturbation is given with the fundamental wave number $\alpha=0.8892$. We give this perturbation an amplitude of 0.01.

In addition to defining the flow scales, we must also discuss our selection of the nondimensional parameters appearing in the final set of equations we use to solve the two-phase flow. This final set of equations consists of Eq. (3) for the bubble phase and Eqs. (9)–(11) for the fluid–bubble mixture. From these equations we have Re, $\mathscr{F}$, and $\bar{\epsilon}$ appearing in the fluid equations and $\mathscr{A}$, $\mathscr{W}$, and $\mathscr{R}$ appearing in the bubble equation as our nondimensional parameters. The mass ratio parameter is fixed at $\mathscr{R}=2$, and to simplify matters we consider an overall void fraction of $\bar{\epsilon}=0.01$ and a Reynolds number of $\mathrm{Re}=1000$ in all cases. This leaves us with $\mathscr{F}$, $\mathscr{A}$, and $\mathscr{W}$. However, these three parameters cannot be chosen independently. We should recognize that both $\mathscr{A}$ and Re give ratios of viscous to inertial forces, likewise $\mathscr{W}$ (actually $\mathscr{W}\cdot\mathscr{A}$) and $\mathscr{F}$ relate gravitational to inertial effects. The difference between these two sets of parameters concerns the length scales on which these terms operate. Therefore, if we include the ratio of bubble to flow length scales, a/δ, in our list of parameters, we can then express the bubble parameters $\mathscr{A}$ and $\mathscr{W}$ in terms of the flow parameters Re and $\mathscr{F}$:

$$\mathscr{A}=\frac{9}{2}\frac{\mathscr{R}}{\mathrm{Re}}\left(\frac{\delta}{a}\right)^2, \tag{12}$$

$$\mathscr{W}=\frac{2}{9}\left(\frac{a}{\delta}\right)^2\left(\frac{3}{2}-\mathscr{R}^{-1}\right)\frac{\mathrm{Re}}{\mathscr{F}^2}. \tag{13}$$

As a result of these relations, for fixed $\bar{\epsilon}$, Re, and $\mathscr{R}$, we have only two independent parameters, and we choose these to be $\mathscr{F}$ and either a/δ or $\mathscr{A}$. By choosing a/δ or $\mathscr{A}$ as a global parameter we are restricting ourselves to simulations with uniform bubble sizes. However, we could easily assign individual values to a/δ (also requiring different values for $\mathscr{A}$ and $\mathscr{W}$) for each bubble in our simulations.

IV. NUMERICAL SIMULATION

The direct numerical simulation used to calculate the evolution of the flow is not unlike methods previously used in Rayleigh–Bénard convection,[21] or more precisely the stratified shear-layer code of Wang and Maxey.[22] We use a pseudospectral technique to advance Eqs. (9)–(11) in our two-dimensional simulations on a 64×128 grid. We simulate a temporal shear layer, and thus apply periodic boundary conditions in the x_1 direction. Because we consider bubbles with a finite rise velocity that can affect the flow, the no normal flow conditions at the vertical boundaries commonly used in the Rayleigh–Bénard simulations are not applicable here. Instead, we apply periodic boundary conditions in the x_3 direction. We do this by extending the domain in x_3 so that flow in the center of the simulation is not influenced by the boundary, and then apply an additional shear layer of the opposite sense to the main shear layer at the boundaries to allow for periodicity. The shear layer at the boundary has twice the thickness of the real shear layer, which in addition to the decay of the initial perturbation away from the central shear layer stabilizes the layer across the boundary. The box size is then $L=2\pi/\alpha\sim7.1$ in the x_1 direction and $2L$ in the x_3 direction.

We rewrite Eq. (10) as follows:

$$\frac{\partial u_i}{\partial t}=(\mathbf{u}\times\boldsymbol{\omega})_i-\frac{\partial}{\partial x_i}\left(P'+\frac{|\mathbf{u}|^2}{2}\right)+\frac{1}{\mathrm{Re}}\frac{\partial^2 u_i}{\partial x_j^2}-\frac{1}{\mathscr{F}^2}\rho'\delta_{3i}, \tag{14}$$

and advance the flow field using a second-order Adams–Bashforth scheme on the nonlinear and buoyancy terms and

Downloaded 22 May 2004 to 128.111.70.70. Redistribution subject to AIP license or copyright, see http://pof.aip.org/pof/copyright.jsp

a second-order Crank–Nicolson scheme on the linear viscous terms. The pressure term and the continuity condition of Eq. (9) are taken care of by projecting the Fourier coefficients of the velocity field onto an incompressible space:

$$\hat{u}_i = \left(\delta_{ij} - \frac{k_i k_j}{|\mathbf{k}|^2} \right) \hat{u}_j ,$$

where k_i is the wave number vector.

We initially seed the entire flow field uniformly with bubbles of the same size, so that the spacing between bubbles in both x_1 and x_3 directions is the same. The bubble locations are advanced by applying the second-order predictor–corrector scheme used in Ruetsch and Meiburg[10] to Eq. (3) after the flow field is advanced. This scheme requires only a first-order accurate estimate of the material derivative of the fluid velocity at both predictor and corrector steps in order to obtain an overall second-order scheme. In order to determine the fluid velocity at the bubble locations, the Hermite interpolation scheme of Balachandar and Maxey[23] is used.

The remaining computational issue concerns the method for obtaining the values for the density at the grid points from the bubble locations. For simulations with bubbles of uniform volume, such as the simulations we consider in this study, we have the relation

$$\epsilon = \eta,$$

where η has been nondimensionalized by $\bar{\eta}$, and thus the perturbation density in Eq. (11) can be expressed as

$$\rho' = \bar{\epsilon}(1-\eta),$$

so that we only need to establish a method of determining the number density at each grid point. In order to do so efficiently, we use an interpolation scheme where a bubble only affects the four grid points that define the cell in which the bubble is located. In general, the contribution of each bubble to these grid points is weighted according to the location of the bubble within the grid cell and the volume of the bubble, but for our uniform bubble size, this contribution is weighted only by the location. For simplicity we use a linear weighting in each direction. Thus, if a bubble is located in a grid cell with the bottom left corner referenced by the grid coordinates (i,j), with the fractional distance of the bubble from this grid point $(\Delta_{x_1},\Delta_{x_3})$, then the contributions from this bubble to the nondimensional number density is given as follows:

$$\eta_{i,j}, \quad (1-\Delta_{x_1})(1-\Delta_{x_3})N_{\mathrm{GRID}}/N_{\mathrm{TOT}},$$

$$\eta_{i+1,j}, \quad \Delta_{x_1}(1-\Delta_{x_3})N_{\mathrm{GRID}}/N_{\mathrm{TOT}},$$

$$\eta_{i+1,j+1}, \quad \Delta_{x_1}\Delta_{x_3}N_{\mathrm{GRID}}/N_{\mathrm{TOT}},$$

$$\eta_{i,j+1}, \quad (1-\Delta_{x_1})\Delta_{x_3}N_{\mathrm{GRID}}/N_{\mathrm{TOT}},$$

where $N_{\mathrm{GRID}}=64\times128$ is the total number of grid points and N_{TOT} is the total number of bubbles in the flow. For an equally spaced grid, we can think of the number density as the number of bubbles/grid cell, in which case the average number density is given by the ratio $N_{\mathrm{TOT}}/N_{\mathrm{GRID}}$, and the local number density is determined by summing the $(1-\Delta_{x_1})(1-\Delta_{x_3})$, etc., terms. The ratio of these gives the nondimensional number density. Even for large numbers of bubbles, this technique creates high frequencies in the Fourier coefficients of the density field, and therefore requires some sort of filtering. We apply an exponential filter to the Fourier coefficients of the density field:

$$\hat{\rho}' = \hat{\rho}' \exp\left[-\gamma \left(\frac{|\mathbf{k}|}{k_{\max}} \right)^4 \right],$$

where γ is chosen so $\exp(-\gamma)$ gives the machine accuracy, and $k_{\max}$ is the maximum wave number in either direction. Since we are dealing with a flow that has a large separation between the wave numbers representing the flow and the noise generated by the projection of bubbles onto the grid points, the choice of the filter does not play a role in the results.

Although we simulate a two-dimensional flow, the void fraction here represents a volumetric void fraction, which can be interpreted by assuming the bubble field is periodic in the x_2 direction with the same initial spacing between bubbles in x_2 as in x_1 and x_3, with the flow uniform in the x_2 direction. We would like to choose a large number of bubbles, which result in smoother density profiles, but at the same time require that ϵ be small. Because we assume that there is no interaction between bubbles in our weakly dilute cases, we satisfy both conditions by carrying "virtual" bubbles along with the "actual" bubbles. The virtual bubbles, which are evenly spaced between the actual bubbles initially, serve as a means of smoothing the density profiles in a meaningful fashion. As a result of carrying along the virtual bubbles, we need to be careful in determining when to use the actual number of bubbles, N_{ACT}, and when to use the total number of bubbles in the simulation, $N_{\mathrm{TOT}}=N_{\mathrm{ACT}}+N_{\mathrm{VIRT}}$. We can obtain a smoother density values at the grid points by summing over all the bubbles and normalizing by N_{TOT}, however, we determine the other parameters of the flow based on N_{ACT}. As an example, we determine the bubble radius from ϵ and N_{ACT}. In turn, the bubble parameters $\mathscr{A}$ and $\mathscr{W}$ are given by this bubble radius and Eqs. (12) and (13). A detailed summary of the parameters for all simulations is given in Table I.

V. ANALYSIS

We begin our analysis of the effect of bubbles on the shear layer by investigating the changes that occur to the vorticity field. The general vorticity equation for a Boussinesq fluid with gravity acting in the negative x_3 direction is given by

$$\frac{D\omega_i}{Dt} = \omega_j \frac{\partial u_i}{\partial x_j} + \frac{1}{\mathscr{F}^2}\left(\frac{\partial \rho'}{\partial x_1}\delta_{i2} - \frac{\partial \rho'}{\partial x_2}\delta_{i1} \right) + \frac{1}{\mathrm{Re}} \frac{\partial^2 \omega_i}{\partial x_j^2} .$$

The first two terms on the right-hand side of this equation are vorticity production terms resulting from vortex stretching/tilting and horizontal density fluctuations being acted on by gravity. The last term represents the viscous diffusion of vorticity. In our case, where we are dealing with only two spatial dimensions, the vorticity equation reduces to

Downloaded 22 May 2004 to 128.111.70.70. Redistribution subject to AIP license or copyright, see http://pof.aip.org/pof/copyright.jsp

TABLE I. Flow and bubble parameters.

Simulation	Re	$\mathscr{F}$	a/δ	$\mathscr{A}$	$\mathscr{W}$	$\tilde{\epsilon}$	N_{TOTAL}	N_{ACT}
I	1000	∞	0.039	5.8	0.34	0.01	294 912	1152
II	1000	∞	0.029	10.3	0.19	0.01	294 912	2048
III	1000	∞	0.019	23.2	0.086	0.01	294 912	4608
IV	1000	1.0	0.039	5.8	0.34	0.01	294 912	1152
V	1000	1.0	0.029	10.3	0.19	0.01	294 912	2048
VI	1000	1.0	0.019	23.2	0.086	0.01	294 912	4608
VII	1000	∞	0.039	5.8	0.68	0.01	294 912	1152
VIII	1000	∞	0.029	10.3	0.38	0.01	294 912	2048
IX	1000	∞	0.019	23.2	0.17	0.01	294 912	4608
X	1000	$1/\sqrt{2}$	0.039	5.8	0.68	0.01	294 912	1152
XI	1000	$1/\sqrt{2}$	0.029	10.3	0.38	0.01	294 912	2048
XII	1000	$1/\sqrt{2}$	0.019	23.2	0.17	0.01	294 912	4608
XIII	1000	∞	0.039	5.8	0.085	0.01	294 912	1152
XIV	1000	∞	0.029	10.3	0.048	0.01	294 912	2048
XV	1000	∞	0.019	23.2	0.022	0.01	294 912	4608
XVI	1000	2.0	0.039	5.8	0.085	0.01	294 912	1152
XVII	1000	2.0	0.029	10.3	0.048	0.01	294 912	2048
XVIII	1000	2.0	0.019	23.2	0.022	0.01	294 912	4608

$$\frac{D\omega}{Dt}=\frac{1}{\mathscr{F}^2}\frac{\partial\rho'}{\partial x_1}+\frac{1}{\mathrm{Re}}\frac{\partial^2\omega}{\partial x_j^2}, \tag{15}$$

where ω here is in the x_2 direction. Therefore, for a two-dimensional flow, the only way the vorticity of a material element can change is either by diffusion or due to the coupling term as a result of the horizontal density gradients. Because the density field is periodic in the x_1 direction, the net production of vorticity across the central shear layer resulting from the coupling term is zero. Therefore, diffusion is the only process that affects the circulation across the shear layer.

In addition to the effect of the bubbles on the shear layer, the two-way coupling will also affect aspects of the bubble motion relative to the passive case. Since the deviation of bubble motion from fluid particles is dominated by the effects of pressure, such as the accumulation of bubbles into regions of low pressure, the effects of coupling on the bubble motion can be examined from the equation governing the pressure field. This equation is obtained by taking the divergence of Eq. (14):

$$\frac{\partial^2}{\partial x_i^2}\left(P'+\frac{\mathbf{u}^2}{2}\right)=\frac{\partial}{\partial x_i}(\mathbf{u}\times\boldsymbol{\omega})_i-\frac{1}{\mathscr{F}^2}\frac{\partial\rho'}{\partial x_3}, \tag{16}$$

where, in addition to the nonlinear terms, the density perturbation provides an extra source to the Poisson equation for the pressure. It is interesting to note from Eqs. (15) and (16) that the horizontal gradients in the density affect the vorticity, while it is the vertical density gradients that affect the pressure.

VI. RESULTS

Throughout this section we are interested not so much in describing how the flow and bubble motion evolve with two-way coupling in absolute terms, but rather how this evolution differs from the one-way coupled or passive case. The idea here is to provide some insight into the differences between these two cases, which can be used to develop models that predict the coupled results based on the knowledge of the passive state. It is for this reason that when we discuss results from coupled simulations, we always compare these to simulations performed with passive bubbles. The passive simulations are run by setting $\mathscr{F}=\infty$, which eliminates the effect of the bubbles on the flow, but by keeping all other parameters, including $\mathscr{W}$, identical to the coupled case. We then can generate spatial fields and statistics based on the differences between the two cases.

Before we discuss the results from the coupled simulations and how they differ from their passive counterparts, we must first review some basic features of what occurs in the passive case. Although the density fields for the passive cases will vary depending on $\mathscr{A}$ and $\mathscr{W}$, the evolution of the vorticity field will not change. We show a time sequence of the vorticity field for the passive case in Fig. 1. From this sequence we observe that the flow remains roughly parallel up to $t\sim10$, at which time we observe the formation of the vortex core due to the Kelvin–Helmholtz instability. During the latter stages of the shear layer development, we observe a roughly circular nature of the flow near the vortex center. Simple model flows reflecting this circular nature have been used to investigate the motion of bubbles in vortical flows. One such model that allows a simple analytical solution to bubble trajectories is that of a solid-body vortex.[10] Two important features obtained from this solution are the equilibrium points, or locations where the bubbles come to rest, and the rate at which the bubbles are captured by the equilibrium points. Without any drag correction, an exponential rate of entrapment or accumulation is observed. This entrapment is a function of $\mathscr{A}$ alone, and reaches an optimal value at $\mathscr{A}\sim1$. In the present study we consider $\mathscr{A}\gg1$, and therefore the general trend we expect is for the accumulation of bubbles to be greater as $\mathscr{A}$ becomes smaller. The location of the equilibrium points is a function of both $\mathscr{A}$ and $\mathscr{W}$. For $\mathscr{W}=0$ the equilibrium point coincides with the vortex center. As $\mathscr{W}$ increases, the equilibrium point moves away from the vortex center along a line whose slope depends on $\mathscr{A}$. For

Downloaded 22 May 2004 to 128.111.70.70. Redistribution subject to AIP license or copyright, see http://pof.aip.org/pof/copyright.jsp

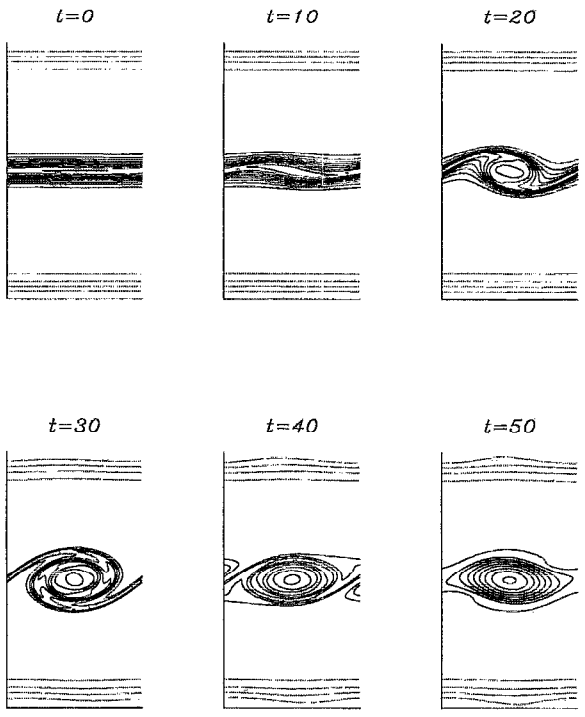

FIG. 1. Time sequence of the vorticity field for passive cases. Contour levels are in increments of 0.1, where solid lines represent positive and dashed lines negative values of vorticity.

large $\mathcal{A}$, this line is roughly horizontal, corresponding to a force balance at the equilibrium point primarily between the drag and gravitational forces.

When the slip velocity of the bubble becomes large, which is most noticeable for cases with rise velocities, we must apply corrections to the Stokes drag assumption, as in Eq. (3). In such cases, the analytical solution for the bubble trajectories discussed above is no longer valid. One important difference between the analytical solution for cases without drag correction and the actual bubble trajectories is the change in entrapment rate near the equilibrium point. The entrapment rate becomes a function of both $\mathcal{A}$ and $\mathcal{F}$, with the entrapment rate decreasing as $\mathcal{F}$ increases. This reduced accumulation rate can be understood by noting that the coefficient of the drag term in Eq. (3) is $f.\mathcal{A}$, where the correction f is a function of the slip velocity. Because the equilibrium point moves farther away from the vortex center with increasing $\mathcal{F}$, the slip velocity at the equilibrium point, $(=u_i)$, and hence f increase accordingly. Therefore, when correcting for the deviation from Stokes drag, we are effectively considering an inertia parameter of $\mathcal{A}_{\mathrm{ACT}}=f_E.\mathcal{A}$, where f_E is the correction at the equilibrium point. Therefore, we expect the bubble accumulation to vary inversely with both $\mathcal{A}$ and $\mathcal{F}$.

Having reviewed these characteristics of the passive bubble motion in a solid-body vortex, we now proceed to discuss the results of the two-way coupled simulations of a bubbly shear layer. In the following sections we group our results according to different Froude numbers, varying the bubble size within each section.

A. $\mathcal{F}=1$: Intermediate case

We begin our analysis for the $\mathcal{F}=1$ cases by considering the largest bubble size, corresponding to an inertia parameter of $\mathcal{A}=5.8$. Up to about $t=20$, we observe small differences between the passive and coupled runs, since during this time the vortex core and pressure gradient have not developed to a point where the bubble accumulation is large enough to affect the flow. At $t=30$, however, we do observe differences between the two cases. A plot of the vorticity, density, and pressure for both passive and coupled cases is shown in Fig. 2(a). It is helpful when comparing the coupled and passive cases to plot the difference between these two fields obtained by subtracting the two fields point by point. These differences are also shown in Fig. 2(a). Consistent with observations from the passive bubble motion in a solid-body vortex, we observe the accumulation of bubbles (signified by a large negative density) to the right of the vortex center. From Eq. (15), we know that such accumulations of bubbles result in vorticity production on either side of the accumulation, given by $\mathcal{F}^{-2}(\partial\rho'/\partial x_1)$. To the left of the accumulation, this term generates negative vorticity and to the right positive vorticity, resulting in the observed decrease of vorticity in the vortex center and the increase in vorticity along the right-hand edge of the vortex.

At later times, such as in Fig. 2(b), we observe a greater change in the vorticity between the passive and coupled cases. Similar to earlier times, the vorticity near the center is reduced while the vorticity near the edge of the vortex is increased. Unlike earlier times, we note that the magnitude of this difference is greatest near the vortex core, and a weaker but more voluminous (positive) difference surrounds the vortex. Statistically, this difference is observed in the PDF of the vorticity difference, $\Delta\omega$, shown in Fig. 3. In this figure, where the vorticity difference is normalized by its RMS value, $\Delta\omega'$, we observe, in addition to the large contribution to the PDF from small values of the vorticity difference, a small peak of negative vorticity difference occurring at $\sim -10\Delta\omega'$. It is these values that correspond to the large vorticity differences near the center of the vortex. There are two reasons for the occurrence of the intense negative vorticity difference and the absence of a similar region of positive vorticity difference. The first is due to the shape of the accumulation region. This region has a sharper gradient on the left side, near the center of the vortex, than on the right side. Although this accumulation region produces no net vorticity, the negative vorticity resulting from the density gradient is more concentrated. The second reason for the absence of a large positive vorticity difference results from the difference in the locations of the equilibrium point of the bubble field and the stagnation point of the flow field. Although the location of bubble accumulation remains approximately stationary throughout the flow evolution, the production of vorticity due to this accumulation applies to material elements of the fluid. The stagnation point in the vortex core occurs to the left of the accumulation region, and therefore the negative vorticity production occurring here is applied to the same fluid elements, resulting in the large negative vorticity difference near the vortex core. To the right of the vortex core the positive vorticity production affects different

Downloaded 22 May 2004 to 128.111.70.70. Redistribution subject to AIP license or copyright, see http://pof.aip.org/pof/copyright.jsp

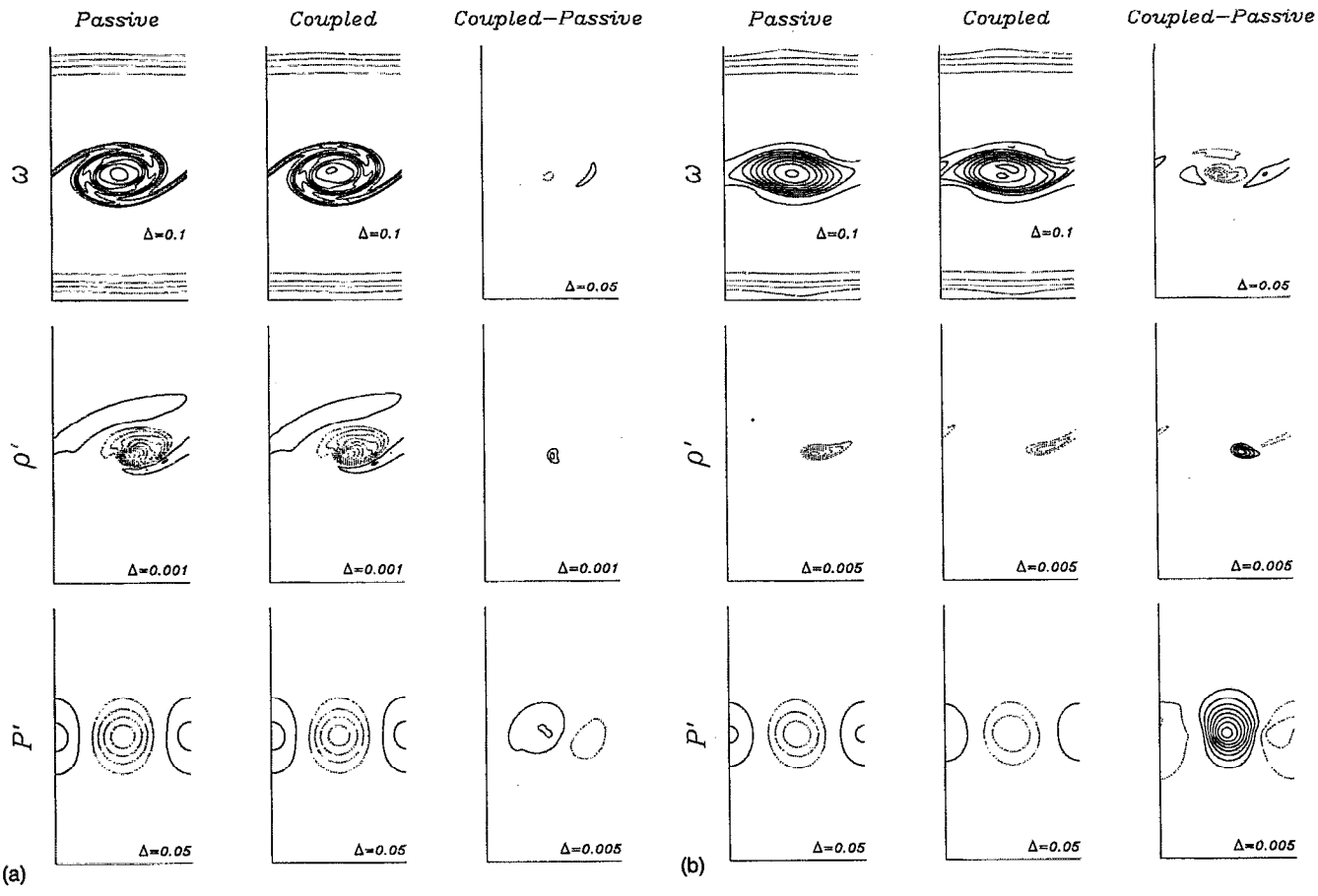

FIG. 2. Vorticity, density, and pressure fields for the coupled and passive cases, along with their differences, at (a) $t=30$ and (b) $t=50$ for $\mathscr{F}=1$ and $\mathscr{A}=5.8$. The solid lines indicate positive values and the dashed line negative values. The increment between contour levels is given in each figure. At $t=30$, the accumulation is not large enough to produce substantial changes from the coupling, however, at $t=50$ we observe differences in all fields, most notably the reduction in vorticity, pressure gradient, and bubble accumulation near the vortex center.

fluid elements as they are swept past the accumulation. This sweeping results in a smaller vorticity difference applied to a larger area.

In addition to the effect of the bubbles on the flow, the modification of the flow has an effect on the entrapment of bubbles. This is more clearly seen at later times, for example, in Fig. 2(b). The difference in the density field can be attributed to the reduction in the magnitude of the pressure at the vortex center. The smaller pressure gradients affect both the location and the entrapment rate into the equilibrium points. The entrapment rate is reduced, and the location is shifted away from the vortex center.

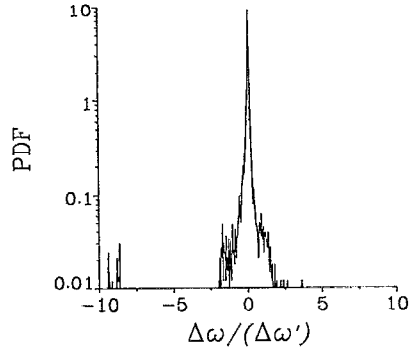

FIG. 3. PDF of relative vorticity between passive and coupled cases at $t=50$ for $\mathscr{F}=1$ and $\mathscr{A}=5.8$. The small peak at large negative values indicates the intensity of the vorticity difference near the vortex center.

Up to this point, we have discussed the basic mechanisms concerning the modification of both flow and bubble fields resulting from two-way coupling for a single set of parameters. As we change the bubble size, and in later sections the Froude number, we observe approximately the same behavior. We therefore focus more on the quantitative changes rather than qualitative features resulting from different parameters. When discussing how different parameters affect the results, we must first discuss what effect the change in parameters has on the passive simulations, and then proceed to the coupled simulations and their difference relative to the passive case.

We now consider smaller bubbles with $\mathscr{A}=10.3$ and 23. In order to keep $\mathscr{F}$ constant, this increase in $\mathscr{A}$ is accompanied by a decrease in $\mathscr{W}$. For the case of passive bubbles in a solid-body vortex we know that the effect of the bubble size on the entrapment rate is twofold. On one hand the entrapment rate decreases with increasing $\mathscr{A}$ for the range of $\mathscr{A}$ considered here. However, we also observe greater accu-

Downloaded 22 May 2004 to 128.111.70.70. Redistribution subject to AIP license or copyright, see http://pof.aip.org/pof/copyright.jsp

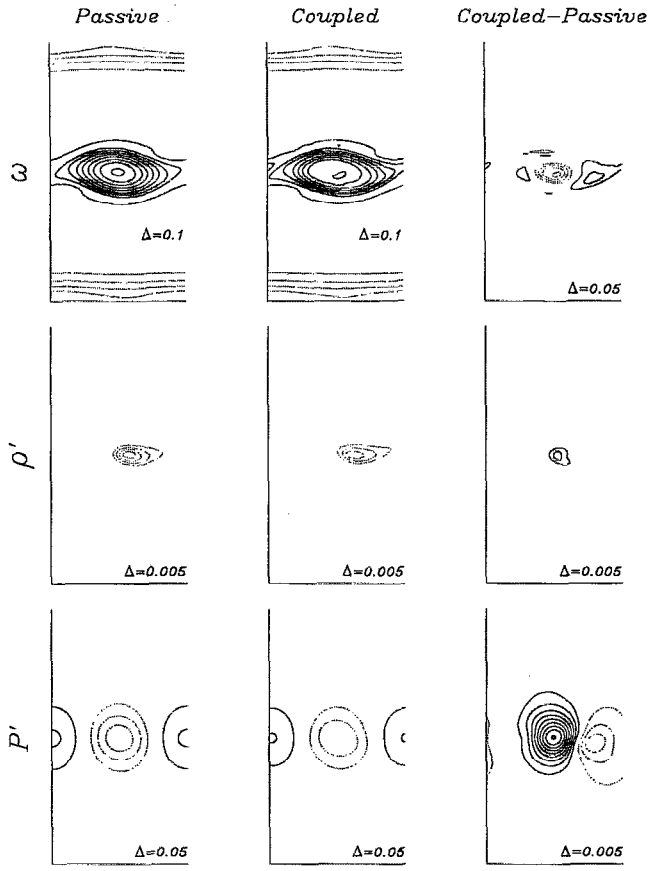

FIG. 4. Vorticity, density, and pressure fields for the coupled and passive cases, along with their differences, at $t=50$ for $\mathscr{F}=1$ and $\mathscr{A}=10.3$. For these smaller bubbles we observe reduced accumulation and hence weaker coupling.

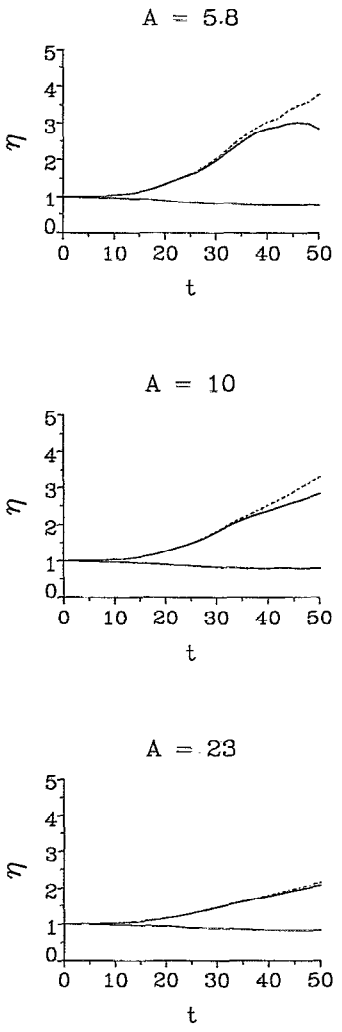

FIG. 5. Time series of maximum and minimum number density, η, for $\mathscr{A}=5.8$ (top), 10.3 (center), and 23 (bottom). All cases have $\mathscr{F}=1$. The solid lines represent two-way coupled and dashed lines passive simulations. These time series show that the accumulation of bubbles decreases with bubble size (larger $\mathscr{A}$). Note that for $\mathscr{A}=5.8$ the maximum accumulation for the coupled case becomes smaller as bubbles are released from the equilibrium points.

mulation rates when $\mathscr{W}$ decreases, since the effective inertia parameter near the equilibrium point is $f_E\mathscr{A}$, and f_E decreases with $\mathscr{W}$. In addition to the effect of bubble size on the entrapment rate, we also observe a shift in the location of the equilibrium point toward the vortex center as the bubble size decreases. We can clearly see these two effects in Fig. 4 for passive bubbles. The accumulation is closer to the center of the vortex relative to the passive case in Fig. 2(b). However, in spite of the reduction of the effective inertia parameter due to the smaller drag correction, we observe a reduced accumulation rate, apparent from the minimum in the ρ' field. The reduction in drag correction does not offset the change in $\mathscr{A}$.

Similar to the case of $\mathscr{A}=5.8$, we observe that the accumulation is smaller and occurs farther away from the vortex center for the coupled simulation than in the passive simulation for these smaller bubbles. However, the degree to which this occurs decreases with smaller bubbles. This difference is quantified in Fig. 5, which shows time series of both the maximum and minimum number densities for all bubble sizes in both passive and coupled simulations. (The minimum in ρ' corresponds to the maximum in η.) From this figure we see that the accumulation decreases with bubble size for the passive and coupled cases. In addition, the difference between the passive and coupled cases also decreases with bubble size. This is what one expects, the largest difference between passive and coupled cases occurs when the density gradient and hence accumulation is largest, which in turn occurs for the larger bubbles. Note that at later times for the case where $\mathscr{A}=5.8$, the reduction of vorticity is so great that the vortex becomes unable to hold all the bubbles it previously entrapped, and as a result the number density decreases, as shown in Fig. 5. As a result, the density minimum for $\mathscr{A}=5.8$ is only slightly larger than for $\mathscr{A}=10.3$, which at the last time frames show a roughly equivalent maximum vorticity difference.

Aside from the two-dimensional contour plots of the density fields and the time series of the maximum and minimum number density, another useful quantity to examine is the vertical profile of the density field, obtained by averaging

Downloaded 22 May 2004 to 128.111.70.70. Redistribution subject to AIP license or copyright, see http://pof.aip.org/pof/copyright.jsp

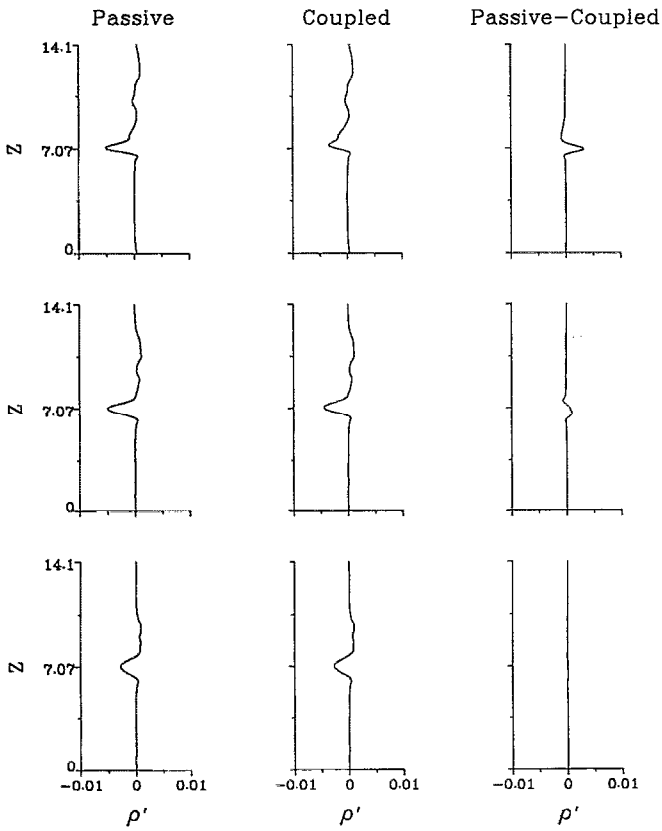

FIG. 6. Vertical density profiles averaged over horizontal slices at $t=50$ for $\mathscr{A}=5.8$ (top), 10.3 (center), and 23 (bottom). All cases have $\mathscr{F}=1$. Here we observe how the accumulation and difference between coupled and passive cases decrease with bubble size.

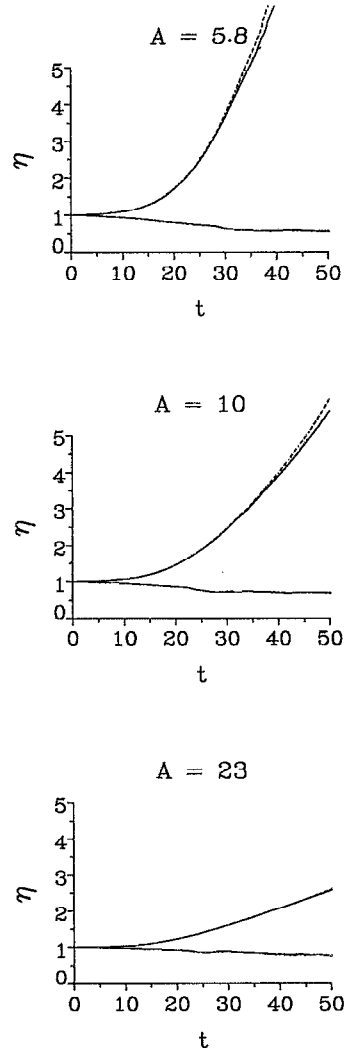

FIG. 7. Time series of maximum and minimum number density for $\mathscr{A}=5.8$ (top), 10.3 (center), and 23 (bottom). All cases have $\mathscr{F}=2$. The solid lines represent two-way coupled and dashed lines passive simulations. The reduced gravitational effects result in much larger accumulations for both passive and coupled cases than for the $\mathscr{F}=1$ cases.

the density over horizontal slices. The advantage of these profiles over the full 2-D fields is that the differences between the passive and coupled density fields due to the shift in the equilibrium point is eliminated, since this shift is primarily horizontal. These profiles also provide more information than the time series of the extremum density values. Such profiles for passive, coupled, and the difference fields for all bubble sizes are shown in Fig. 6. Here we observe that as the bubble size decreases the spike representing accumulation of bubbles decreases and becomes broader. More striking is the reduction in the difference profile with decreasing bubble size.

B. $\mathscr{F}=2$: Weak gravity

If we now consider larger values of $\mathscr{F}$, we reduce the gravitational effects on the flow and bubbles. In terms of the bubble parameters, for the same bubble sizes as in the previous section we maintain the same values of $\mathscr{A}$, but have smaller values of $\mathscr{W}$. The effect these smaller rise velocities have on the accumulation of bubbles in the passive case is to move the equilibrium points closer to the vortex center and to increase the entrapment rate, as seen in Fig. 7. The increase in entrapment rate is most noticeable for the larger bubbles, with $\mathscr{A}=5.8$, where the maximum number density reaches values of $\sim 20\bar{\eta}$. These large accumulation rates can be attributed to the smaller correction to the Stokes drag due to the proximity of the equilibrium points to the vortex center.

In the coupled simulations with $\mathscr{F}=2$, we also observe a larger accumulation of bubbles than in the coupled simulations with $\mathscr{F}=1$. One might have expected that the large accumulations, especially in the $\mathscr{A}=5.8$ case, would alter the pressure field to the extent that the accumulation rate would be drastically reduced, even to the point where the accumulation itself decreases, as in the latter stages in the $\mathscr{F}=1$ and $\mathscr{A}=5.8$ case. However, when comparing simulations with different Froude numbers, we must remember that the effect of bubble accumulation on the pressure and vorticity fields is dependent not only on the magnitude of the density gradients, but also in the Froude number through the $\mathscr{F}^{-2}$ coefficient. As a result, although we see a greater accumulation of bubbles for the $\mathscr{F}=2$ case than in the $\mathscr{F}=1$ case,

Downloaded 22 May 2004 to 128.111.70.70. Redistribution subject to AIP license or copyright, see http://pof.aip.org/pof/copyright.jsp

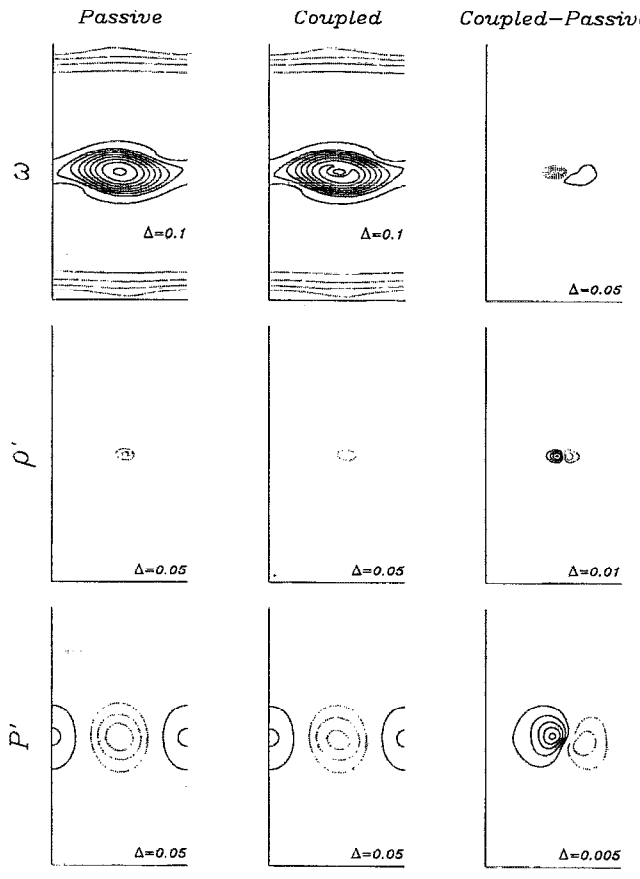

FIG. 8. Vorticity, density, and pressure fields for the coupled and passive cases, along with their differences, at $t=50$ for $\mathcal{F}=2$ and $\mathcal{A}=5.8$. For this larger Froude number and hence smaller rise velocity, the bubbles accumulate more toward the vortex center with an enhanced accumulation rate.

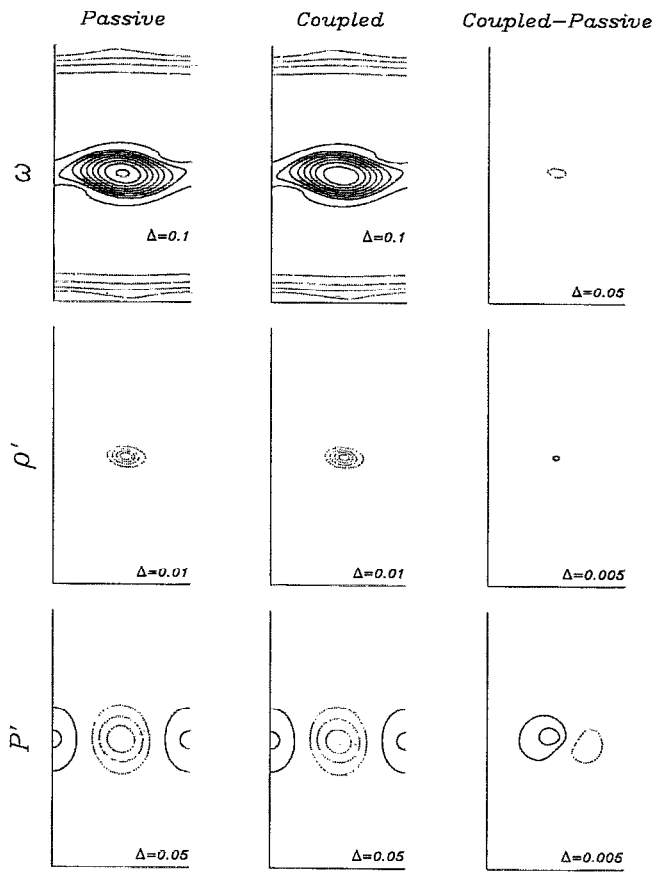

FIG. 9. Vorticity, density, and pressure fields for the coupled and passive cases, along with their differences, at $t=50$ for $\mathcal{F}=2$ and $\mathcal{A}=10.3$. Although the accumulation is greater than for the same sized bubbles with $\mathcal{F}=1$, due to the $\mathcal{F}^{-2}$ coefficient the coupling effects are smaller.

the pressure gradients for the $\mathcal{F}=2$, $\mathcal{A}=5.8$ case, shown in Fig. 8, are affected less by the bubble accumulation than in the $\mathcal{F}=1$ case of Fig. 2(b). From Fig. 8 we notice that the change in the vorticity field between passive and coupled cases is larger in magnitude than for the $\mathcal{F}=1$ case, although the difference is confined to a smaller region. Therefore we have a large difference in vorticity near the vortex center, but elsewhere the vorticity field is not affected.

As we look at smaller bubbles for the $\mathcal{F}=2$ case, the accumulation rate decreases for both passive and coupled cases. Although $\eta_{\max}$ is greater here than in their $\mathcal{F}=1$ counterparts, the smaller coefficient of the density gradient terms in the vorticity and pressure equations begins to take effect, resulting in very small differences between the passive and coupled cases, as seen in Fig. 9. In addition to the small differences in the vorticity and pressure fields, we also observe similar trends in the density fields between passive and coupled cases. In fact, the large difference in the density field between the passive and coupled cases in Fig. 8 is attributed primarily to the slight shift in the equilibrium point. We can get a better view of this by examining the vertical density profiles in Fig. 10. Here we see that although the density near the equilibrium points is much smaller than in the $\mathcal{F}=1$ case (note the different horizontal scale in Fig. 6 and Fig. 10), the difference between the passive and coupled simulations for all bubbles sizes is much smaller for $\mathcal{F}=2$.

C. $\mathcal{F}=0.707$: Strong gravity

One might expect from the results with $\mathcal{F}=2$ and 1 that as we consider $\mathcal{F}<1$, where gravitational effects are larger, we would observe smaller accumulation rates but with enhanced vorticity production. In the previous sections the coefficient of the vorticity production term, $\mathcal{F}^{-2}$, was for the most part dominant over the changes in the accumulation rate of bubbles. Although we do see the accumulation of bubbles decreasing with increasing rise velocity, we observe another phenomenon which reduces vorticity production. This is depicted in Figs. 11(a)–11(c). At time $t=30$, we observe the accumulation of bubbles similar to the cases with large Froude numbers, but at times $t=40,50$ the bubbles leave this accumulation region as they advect with the fluid and rise velocities. The pressure gradients near the vortex center are smaller at these later times, and as a result the vortex is no longer able to trap bubbles. Note that this occurs in both passive and coupled cases, and therefore is not a result of the two-way coupling between phases. A similar phenomenon was observed in passive bubbles rising through steady-state Stuart vortices.[10] In the Stuart vortex flow for

Downloaded 22 May 2004 to 128.111.70.70. Redistribution subject to AIP license or copyright, see http://pof.aip.org/pof/copyright.jsp

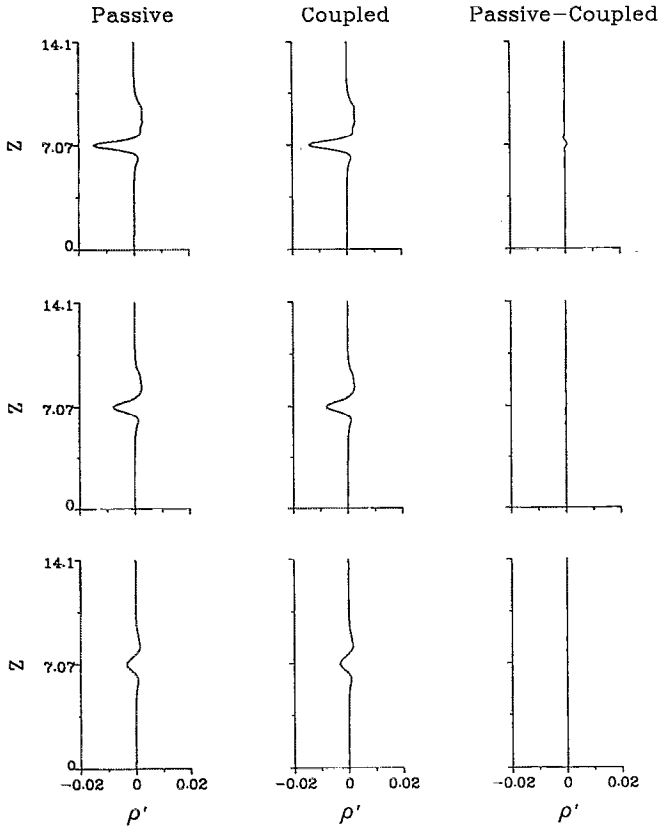

FIG. 10. Vertical density profiles averaged over horizontal slices at $t=50$ for $\mathcal{A}=5.8$ (top), 10.3 (center), and 23 (bottom). All cases have $\mathcal{F}=2$. The *passive-coupled* column clearly shows the weaker coupling effects relative to Fig. 6.

cases without equilibrium points there exists a point that is least unstable and allows bubbles to be retained by the flow, but not trapped. The motion of bubbles in our unsteady flow results from both the disappearance of the equilibrium point and to a lesser extent the retention of bubbles near a least unstable point. As the bubbles are released from this region, they form streaks that advect with the fluid and rise velocities.

The effect of these streaks on the maximum bubble concentration is shown in Fig. 12. For the largest bubbles, the maximum number density only reaches $\sim 1.5\tilde{\eta}$. After $t\sim 30$ the maximum number density actually decreases for both passive and coupled cases. Because of these small accumulations, we see from Figs. 11(a)–11(c) that there is little difference between the vorticity and pressure fields of the passive and coupled simulations. As a result, the number density fields of both passive and coupled simulations are roughly the same. Note that unlike cases with stable equilibrium points, the vorticity production in this case occurs along the streaks of bubbles and not near the vortex center.

As we consider smaller bubbles at the same Froude number, the decrease in rise velocity accompanying the difference in size results in the reappearance of the equilibrium point during the latter stages. As a result, we observe larger accumulations of bubbles, with greater differences between passive and coupled cases, as demonstrated in Figs. 12 and 13. However, once the rise velocity is small enough to create an equilibrium point, as in the case for $\mathcal{A}=10.3$, then as we move to smaller bubbles and thus rise velocities, such as those with $\mathcal{A}=20$, we once again find that the accumulation decreases due to larger drag, and the difference between passive and coupled cases becomes smaller. This suggests that at some intermediate bubble size there is an optimum coupling effect. For large bubbles, there is no equilibrium point and hence no large accumulation, and for small bubbles the accumulation rate into the equilibrium point is so small that large density gradients are not produced. The reason no such trend was observed for larger Froude numbers is due to restriction on bubble size needed to satisfy our assumptions.

VII. DISCUSSION AND CONCLUSIONS

Through direct numerical simulations we have obtained information regarding the effect of two-way coupling of bubbly flows with dilute concentrations of bubbles. In general, we are interested in how the two-way coupled simulations affect both bubble and flow motion relative to the passive case. To summarize the results of the previous sections, we find that the vorticity near the center of the vortex is reduced as a result of the accumulation of bubbles, and that the pressure gradients near the vortex center are also reduced, resulting in a smaller accumulation for the coupled simulations relative to the passive case. We have explored how the bubble size and Froude number affect these changes. In general, we notice smaller coupling effects for smaller bubbles, since the accumulation rate decreases with bubble size. For most of the the simulations considered here, the effect of the Froude number on the results is dominated by the $\mathcal{F}^{-2}$ coefficient in the vorticity production and pressure equations rather than the effect of the Froude number on the accumulation rate.

Although we have only considered the bubble size and Froude numbers as parameters in this study, the information we obtained from this can explain how changes in other parameters affect the results. We have used a constant void fraction in this study, but if we substitute the equation for the perturbation density into the momentum equation, we see that the coefficient of the coupling terms can be expressed as $\tilde{\epsilon}/\mathcal{F}^2$. Thus, changes in the global void fraction can be explained directly from the previous results. Moderate changes in the Reynolds number do not effect the flow greatly, but would alter the values of $\mathcal{A}$ and $\mathcal{W}$ via Eqs. (12) and (13).

In addition to the effects of different parameters on the simulations, we should also consider how different configurations may affect the results. In this study we have only presented material corresponding to flows uniformly seeded with uniform bubble sizes. We have also run simulations with variable bubbles sizes, ranging the entire scope of bubbles considered in this study. In general, the results are similar to what is observed for uniform bubbles sizes, except that the accumulation region is not as compact and the changes in the pressure and vorticity fields not as great due to the smaller density gradients.

Regardless of the values of the parameters, one recurring theme in the simulations is that in most cases an equilibrium

Downloaded 22 May 2004 to 128.111.70.70. Redistribution subject to AIP license or copyright, see http://pof.aip.org/pof/copyright.jsp

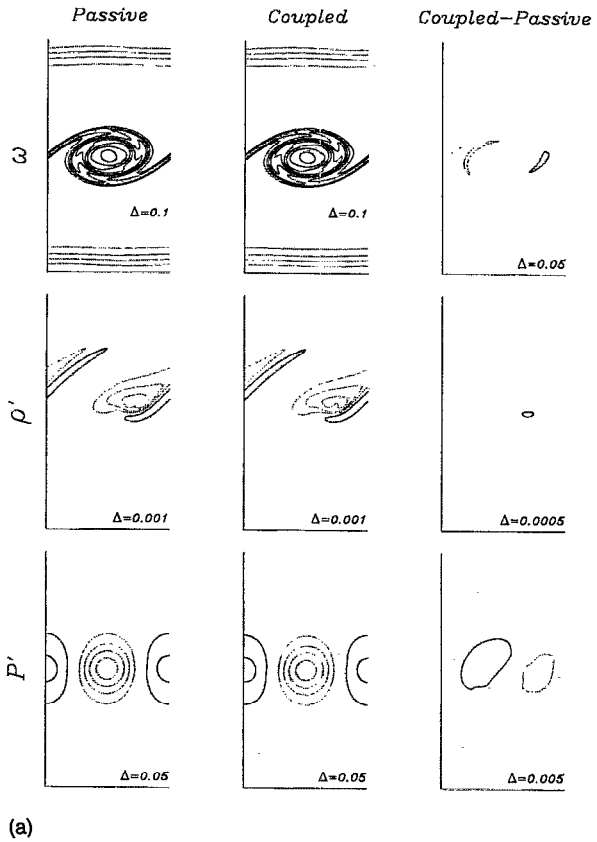

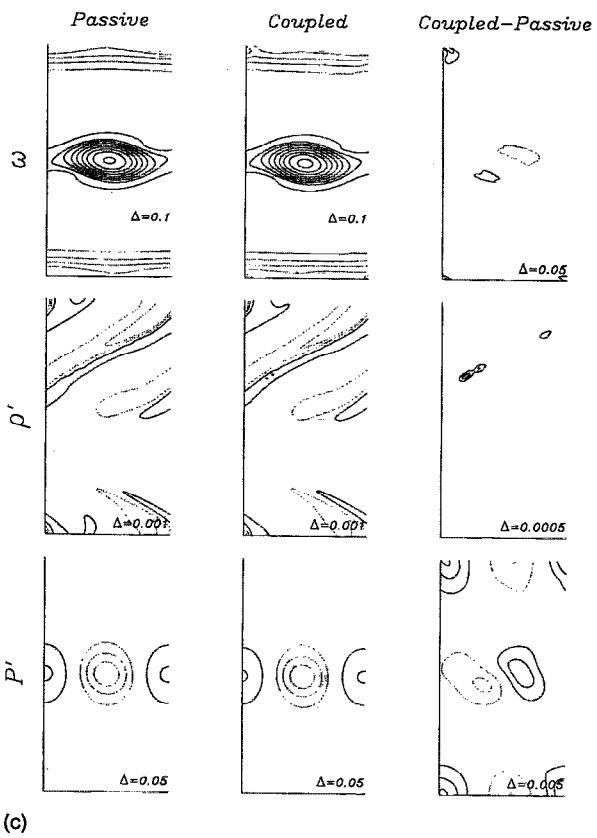

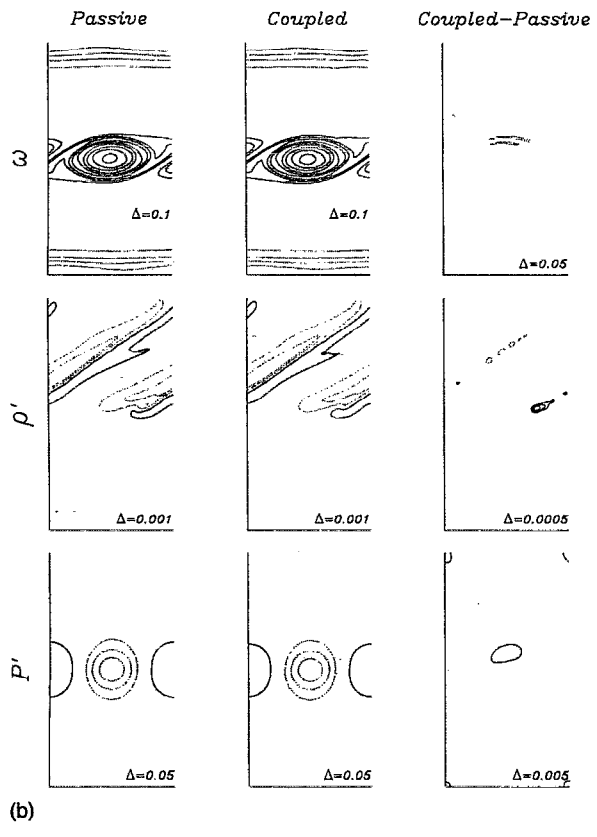

FIG. 11. Vorticity, density, and pressure fields for the coupled and passive cases, along with their differences, for $A=5.8$ and $\mathcal{F}=0.707$ at (a) $t=30$, (b) $t=40$, and (c) $t=50$. Although we see the accumulation of bubbles similar to previous cases at $t=30$, at later times the pressure gradient is not large enough to entrap bubbles, and as a result we observe streaks of bubbles that are produced from a least unstable point replacing the equilibrium point.

Downloaded 22 May 2004 to 128.111.70.70. Redistribution subject to AIP license or copyright, see http://pof.aip.org/pof/copyright.jsp

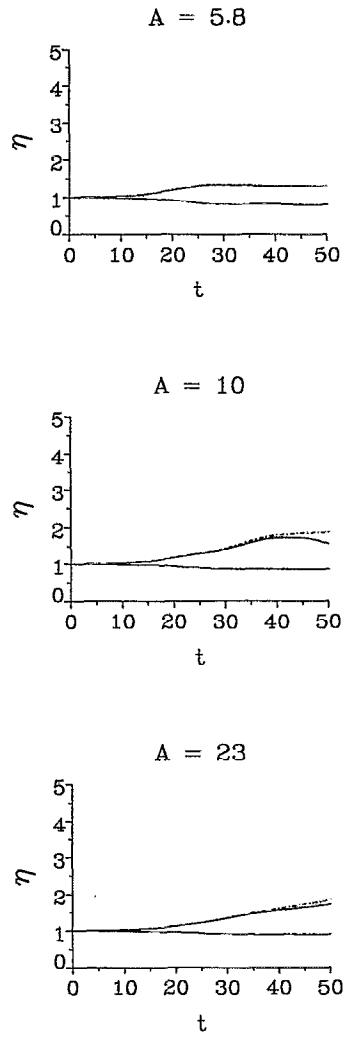

FIG. 12. Time series of maximum and minimum number density for $\mathcal{A}=5.8$ (top), 10.3 (center), and 23 (bottom). All cases have $\tilde{\mathcal{F}}=0.707$. The solid lines represent two-way coupled and dashed lines passive simulations. The larger gravitational effects result in smaller accumulations, most noticeable in the $\mathcal{A}=5.8$ case, where there is no equilibrium point for the bubbles at later times.

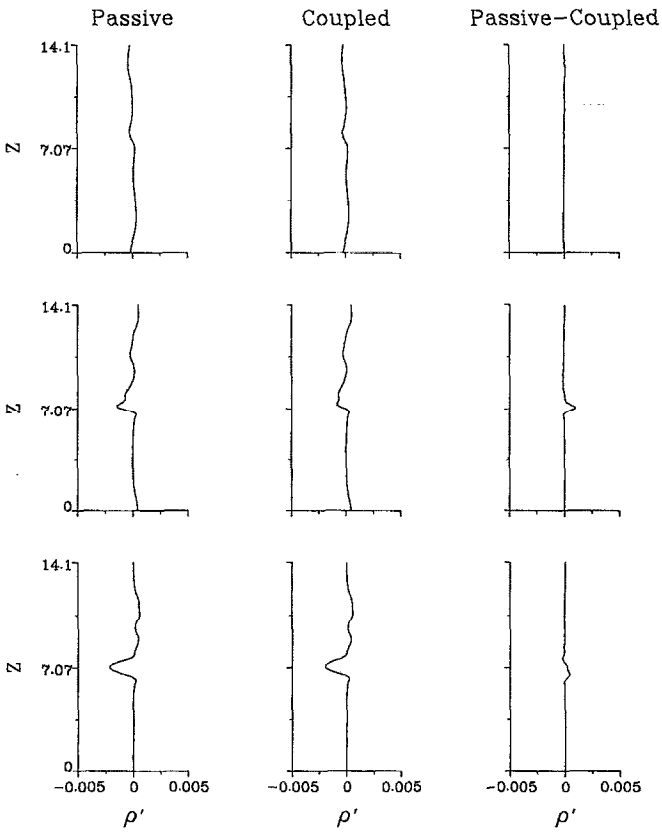

FIG. 13. Vertical density profiles averaged over horizontal slices at $t=50$ for $\mathcal{A}=5.8$ (top), 10.3 (center), and 23 (bottom). All cases have $\tilde{\mathcal{F}}=0.707$. This suggests that there is an optimum bubble size in terms of bubble accumulation for cases with small $\tilde{\mathcal{F}}$. For the smallest bubbles (bottom) the accumulation rate is small, but for large bubbles (top) the rise velocity is so large that equilibrium points do not exist.

point exists in the flow where bubbles accumulate. The presence of such a point might seem contrary to the assumption of a dilute bubbly flow. We have chosen a small void fraction and small enough bubbles in the hopes of avoiding violation of the dilute assumption, and we now determine how valid this assumption is. A violation of the weakly dilute assumption would imply that bubbles are close enough that bubble–bubble interactions become important. Although we know of no precise minimum cutoff for the bubble separation to exclude any such interaction, we can easily calculate the minimal bubble separation occurring in the flow at any time simply from the knowledge of the maximum void fraction or number density. The separation between bubble centers, Δs, is given by

$$\frac{\Delta s}{a}=\left(\frac{4\pi}{3\hat{\epsilon}\epsilon}\right)^{1/3}.$$

At the beginning of the simulations, with $\epsilon=1$, we have a uniform separation of $\Delta s/a\sim 7.4$. For all but one simulation, the maximum void fraction is ~ 5, giving $\Delta s/a=4.3$. Although there will be interaction among bubbles in these worst case scenarios, the fact that these regions represent equilibrium points where the absolute and relative bubble velocities are small suggests that the qualitative nature of the flow will not be greatly affected by the interaction.

ACKNOWLEDGMENTS

The authors would like to thank F. K. Browand and M. R. Maxey for their useful discussions, and L.-P. Wang for use of his stratified shear layer code. This work is supported by the Office of Naval Research and simulations were performed at the San Diego Supercomputer Center.

[1] G. L. Brown and A. Rosko, "On density effects and large structure in turbulent mixing layers," J. Fluid Mech. **64**, 775 (1974).
[2] C. D. Winant and F. K. Browand, "Vortex pairing: The mechanism of turbulent mixing layer growth at moderate Reynolds numbers," J. Fluid Mech. **63**, 327 (1974).
[3] R. T. Pierrehumbert and S. E. Widnall, "The two- and three-dimensional instabilities of a spatially periodic shear layer," J. Fluid Mech. **114**, 59 (1982).
[4] W. T. Ashurst and E. Meiburg, "Three-dimensional shear layers via vortex dynamics," J. Fluid Mech. **180**, 87 (1988).

Downloaded 22 May 2004 to 128.111.70.70. Redistribution subject to AIP license or copyright, see http://pof.aip.org/pof/copyright.jsp

[5]B. J. Lázaro and J. C. Lasheras, "Particle dispersion in the developing free shear layer. Part 1: Unforced flow," J. Fluid Mech. **235**, 143 (1992).
[6]B. J. Lázaro and J. C. Lasheras, "Particle dispersion in the developing free shear layer. Part 2: Forced flow," J. Fluid Mech. **235**, 179 (1992).
[7]J. E. Martin and E. Meiburg, "The accumulation and dispersion of heavy particles in forced two-dimensional mixing layers. Part 1: The fundamental and subharmonic cases," Phys. Fluids **6**, 1116 (1994).
[8]C. T. Crowe, R. A. Gore, and T. R. Troutt, "Particle dispersion by coherent structures in free shear flows," Part. Sci. Technol. **3**, 149 (1985).
[9]M. R. Maxey, "The motion of small spherical particles in a cellular flow field," Phys. Fluids **30**, 1915 (1987).
[10]G. R. Ruetsch and E. Meiburg, "On the motion of small spherical bubbles in vortical flows," Phys. Fluids A **5**, 2326 (1993).
[11]A. Biesheuvel and W. C. M. Gorissen, "Void fraction disturbances in a uniform bubbly fluid," Int. J. Multiphase Flow **16**, 211 (1990).
[12]T. L. Cook and F. H. Harlow, "Vortices in bubbly two-phase flow," Int. J. Multiphase Flow **12**, 35 (1986).
[13]K. D. Squires and J. K. Eaton, "Particle response and turbulence modification in isotropic turbulence," Phys. Fluids A **2**, 1191 (1990).
[14]S. Elghobashi and G. C. Truesdell, "On the two-way interaction between homogeneous turbulence and dispersed solid particles. I: Turbulence modification," Phys. Fluids A **5**, 1790 (1993).
[15]H. Clift, J. R. Grace, and M. E. Weber, *Bubbles, Drops, and Particles* (Academic, New York, 1978).
[16]G. K. Batchelor, *An Introduction to Fluid Dynamics* (Cambridge University Press, Cambridge, 1967).
[17]M. R. Maxey and J. J. Riley, "Equation of motion for a small rigid sphere in a non-uniform flow," Phys. Fluids **26**, 883 (1983).
[18]T. R. Auton, J. C. R. Hunt, and M. Prud'homme, "The forces exerted on a body in inviscid unsteady non-uniform rotational flow," J. Fluid Mech. **197**, 241 (1988).
[19]R. Mei, C. J. Lawrence, and R. J. Adrian, "Unsteady drag on a sphere at finite Reynolds number with small fluctuations in the free-stream velocity," J. Fluid Mech. **233**, 613 (1991).
[20]A. Michalke, "On the inviscid instability of the hyperbolic-tangent velocity profile," J. Fluid Mech. **19**, 543 (1964).
[21]S. Balachandar, M. R. Maxey, and L. Sirovich, "Numerical simulation of high Rayleigh number convection," J. Sci. Comput. **4**, 219 (1989).
[22]L.-P. Wang and M. R. Maxey, "Kinematical descriptions for mixing in stratified or homogeneous shear flows," in *Mixing in Geophysical Flows—Effects of Body Forces in Turbulent Flows*, edited by J. M. Redondo and O. Metais, Universitat Politecnica de Catalunya, Barcelona, December 1992 (Kluwer, Dordrecht, 1993).
[23]S. Balachandar and M. R. Maxey, "Methods for evaluating fluid velocities in spectral simulations of turbulence," J. Comput. Phys. **79**, 96 (1989).

Downloaded 22 May 2004 to 128.111.70.70. Redistribution subject to AIP license or copyright, see http://pof.aip.org/pof/copyright.jsp